PHYSICAL REVIEW D **96,** 066013 (2017)

Approaching confinement structure for light quarks in a holographic soft wall QCD model

Meng-Wei Li,[1,†] Yi Yang,[2,*] and Pei-Hung Yuan[1,‡]

[1]*Institute of Physics, National Chiao Tung University, Hsinchu 300, Republic of China*
[2]*Department of Electrophysics, National Chiao Tung University, Hsinchu, Taiwan 300, Republic of China*

(Received 12 June 2017; published 12 September 2017)

We study the confinement-deconfinement phase transition in a holographic soft-wall QCD model. By solving the Einstein-Maxwell-scalar system analytically, we obtain the phase structure of the black hole backgrounds. We then impose probe open strings in such a background to investigate the confinement-deconfinement phase transition from different open string configurations under various temperatures and chemical potentials. Furthermore, we study the Wilson loop by calculating the minimal surface of the probing open string world sheet and obtain the Cornell potential in the confinement phase analytically.

DOI: 10.1103/PhysRevD.96.066013

I. INTRODUCTION

There are various phase structure phenomena in quantum chromodynamics (QCD) theory. The confinement-deconfinement phase transition is one of the most important phenomena in the QCD phase diagram. It is widely believed that the system is in the confinement phase in the low temperature T and small chemical potential μ (low quark density) region, in which quarks are confined to hadronic bound states, e.g., mesons and baryons. On the other hand, it is in the deconfinement phase in the high temperature and large chemical potential (high quark density) region, in which free quarks exist, e.g., the quark gluon plasma. It is natural to conjecture that there exists a phase transition between the two phases, as shown in Fig. 1(a) (carton phase diagram at $m = 0$).

Understanding the confinement-deconfinement phase transition in QCD is a very important but extremely difficult task. The interaction becomes strong around the phase transition region, so that the conventional perturbation method in quantum field theory does not work. For a long time, lattice QCD was the only method to attack the problem of phase transitions in QCD [2,3]. According to the calculation in lattice QCD, the confinement-deconfinement phase transition is first order in the zero-quark-mass limit $m_q = 0$. However, with a finite quark mass a part of the phase transition line would become a crossover. For small and large quark masses, the behaviors of the phase transformation at zero chemical potential ($\mu = 0$) have been calculated using lattice QCD. The phase diagrams are conjectured and shown (carton phase diagrams at finite m) for a light quark and a heavy quark in Figs. 1(b) and 1(c), respectively.

*Corresponding author.
yiyang@mail.nctu.edu.tw
†sr755332@gmail.com
‡phy.pro.phy@gmail.com

However, lattice QCD faces the so-called sign problem at finite chemical potential. To study the full phase structure in QCD, we need new methods. During the last 15 years, the AdS/CFT duality has been developed in string theory [4]. Using this duality, the quantum properties in a conformal field theory can be investigated by studying its dual string theory in an anti–de Sitter (AdS) background. Lately, the AdS/CFT duality has been generalized and applied to nonconformal field theory including QCD, namely, AdS/QCD or holographic QCD [5–26]. Holographic QCD offers a suitable frame to study phase transitions in QCD at all temperatures and chemical potentials. There are two types of holographic QCD models, i.e., top-down and bottom-up models. In this work, we will study a bottom-up model based on the soft-wall model [11], which is the first holographic QCD model realizing the linear Regge spectrum of mesons [27]. The holographic QCD model to describe heavy quarks was constructed in Ref. [24]. The meson Regge spectrum and phase structure in QCD were studied by analytically solving the full backreacted Einstein equation. In Refs. [28–40], a probe open string in an AdS background was studied. In Ref. [26], probe open strings were added to the holographic QCD model for heavy quarks and the behavior of open strings was studied in the black hole background. By combining the various open string configurations and the phase structure of the black hole background, a new physical picture of the phase diagram for the confinement-deconfinement phase transition in holographic QCD was suggested. A holographic QCD model to describe light quarks was also studied in Ref. [25]; however, the scalar field becomes complex, which causes some problems.

In this work, we construct a bottom-up holographic QCD model by studying its dual five-dimensional gravity theory coupled to an Abelian gauge field and a neutral scalar field, i.e., the Einstein-Maxwell-scalar system (EMS). We

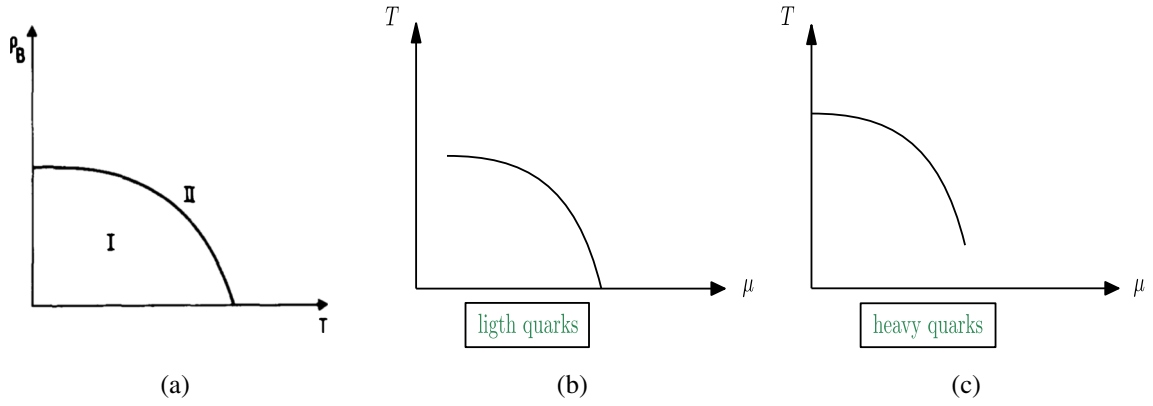

(a) (b) (c)

FIG. 1. (a) The first schematic QCD phase diagram of hadronic matter claimed by Cabibbo and Parisi in 1975, where ρ_B labels the baryon density. The transition line divided the phase space into two phases. Quarks are bounded in phase I and unconfined in phase II [1]. (b) Nowadays, lattice simulations have convinced people that the QCD phase diagram behaves as (a) in the chiral limit, but a crossover regime exists for massive cases. A light-quark phase transition should look similar to panel (b); otherwise, it would resemble panel (c) when considering heavy quarks even the pure gauge limit.

analytically solve the equations of motion to obtain a family of black hole backgrounds which depend on two arbitrary functions $f(z)$ and $A(z)$. Since one of the crucial properties for soft-wall holographic QCD models is that the vector-meson spectrum satisfies the linear Regge trajectories at zero temperature and zero density, we are able to fix the function $f(z)$ by requiring the linear meson spectrum. Then, by choosing a suitable function $A(z)$, we obtain a black hole background which appropriately describes many important properties in QCD. We explore the phase structure of the black hole background by studying its thermodynamic quantities under different temperatures and chemical potentials. In addition, we study the Wilson loop [41] and the light quark potential in our holographic QCD model by putting a probe open string in the black hole background and studying the dynamics of the open string. We find three configurations for the open string in a black hole, as in Fig. 2. Combining the background phase structure and the open string breaking effect, we obtain the phase diagram for the confinement-deconfinement transition.

The paper is organized as follows. In Sec. II, we review the EMS system and obtain a family of analytic black hole background solutions. We study the thermodynamics of the black hole backgrounds to get their phase structure in Sec. III. We add a probe open string to the black hole background to study their various configurations. We calculate the expectation value of the Wilson loop and study the quark potential in Sec. IV. By combining the background phase structure and the open string breaking effect, we obtain the phase diagram for the confinement-deconfinement transition in Sec. V. We conclude with our results in Sec. VI.

II. EINSTEIN-MAXWELL-SCALAR SYSTEM

The EMS system has been widely studied in constructing bottom-up holographic QCD models. In this section, we

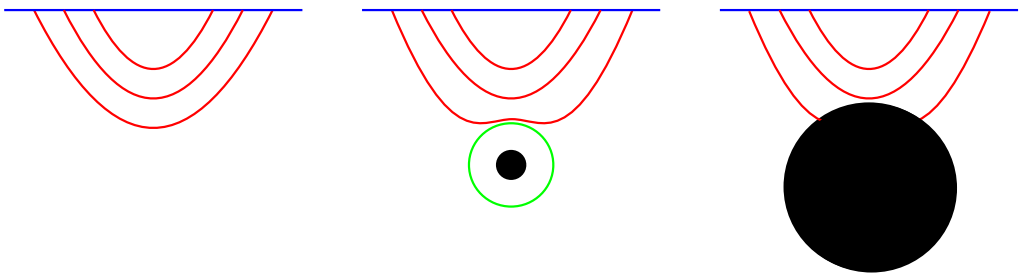

(a) (b) (c)

FIG. 2. Three configurations for open strings in a black hole background. When the black hole is absent (a), open strings are always connected with two ends attached on the AdS boundary. In the small black hole case (b), the strings cannot exceed a certain depth from the boundary and are still connected, with their two ends on the AdS boundary. For the large black hole case (c), the open strings with their two ends separated enough will break into two open strings where one end stays on the AdS boundary and the other falls into the black hole horizon.

briefly review the EMS and, by solving the equations of motion analytically, we obtain a family of black hole solutions which we have previously studied in Refs. [24–26].

A. String frame and Einstein frame

We consider a five-dimensional EMS system with probe matter fields. The system can be described by an action with two parts: a background sector S_B and a matter sector S_m,

$$S = S_B + S_m. \tag{2.1}$$

In the string frame (labeled by a subindex s), the background part S_B includes a gravity field $g^s_{\mu\nu}$, a Maxwell field A_μ, and a neutral scalar field ϕ^s,

$$S_B = \frac{1}{16\pi G_5}\int d^5x\sqrt{-g^s}e^{-2\phi^s} \times\left[R^s - \frac{f^s_B(\phi^s)}{4}F^2 + 4\partial_\mu\phi^s\partial^\mu\phi^s - V^s(\phi^s)\right], \tag{2.2}$$

where G_5 is the five-dimensional Newtonian constant, $F_{\mu\nu} = \partial_\mu A_\nu - \partial_\nu A_\mu$ is the gauge field strength corresponding to the Maxwell field, $f^s_B(\phi^s)$ is the gauge kinetic function associated to the Maxwell field, and $V^s(\phi^s)$ is the potential of the scalar field. The matter part S_m of the EMS system includes massless gauge fields A^V_μ and $A^{\tilde{V}}_\mu$, which are treated as probes in the background, describing the degrees of freedom of vector mesons and pseudovector mesons on the four-dimensional boundary,

$$S_m = -\frac{1}{16\pi G_5}\int d^5x\sqrt{-g^s}e^{-2\phi^s}\left[\frac{f^s_m(\phi^s)}{4}(F^2_V + F^2_{\tilde{V}})\right], \tag{2.3}$$

where $f^s_m(\phi^s)$ is the gauge kinetic function of the gauge fields A^V_μ and $A^{\tilde{V}}_\mu$. It is worth mentioning that the gauge kinetic functions f^s_B and f^s_m are positive-defined and are not necessary to be the same. For simplicity, in this paper we set $f^s_B = f^s_m = f^s$. We have constructed the EMS system in the string frame, in which it is natural to impose the physical boundary conditions when solving the background solution according to the AdS/CFT dictionary. However, it is more convenient to solve the equations of motion and study the thermodynamical properties of QCD in the Einstein frame.

The string frame action is characterized by the exponential dilaton factor in front of the Einstein term, i.e., $e^{-2\phi^s}R^s$. To transform the action from string frame to Einstein frame, in which the Einstein term is expressed in the conventional form, we make the following Weyl transformations,

$$\phi^s = \sqrt{\frac{3}{8}}\phi, \quad g^s_{\mu\nu} = g_{\mu\nu}e^{\sqrt{\frac{2}{3}}\phi}, \quad f^s(\phi^s) = f(\phi)e^{\sqrt{\frac{2}{3}}\phi}, \quad V^s(\phi^s) = e^{-\sqrt{\frac{2}{3}}\phi}V(\phi). \tag{2.4}$$

Thus, in the Einstein frame, the actions in Eqs. (2.2)–(2.3) become

$$S_B = \frac{1}{16\pi G_5}\int d^5x\sqrt{-g} \times\left[R - \frac{f(\phi)}{4}F^2 - \frac{1}{2}\partial_\mu\phi\partial^\mu\phi - V(\phi)\right], \tag{2.5}$$

$$S_m = -\frac{1}{16\pi G_5}\int d^5x\sqrt{-g}\left[\frac{f(\phi)}{4}(F^2_V + F^2_{\tilde{V}})\right]. \tag{2.6}$$

B. Black hole solution

Now we are able to derive the equations of motion of our EMS system from Eqs. (2.5)–(2.6). We first study the background by turning off the probe matter of the vector field A^V_μ and pseudovector field $A^{\tilde{V}}_\mu$. The equations of motion can be derived as

$$\nabla^2\phi = \frac{\partial V}{\partial\phi} + \frac{F^2}{4}\frac{\partial f}{\partial\phi}, \tag{2.7}$$

$$\nabla_\mu[f(\phi)F^{\mu\nu}] = 0, \tag{2.8}$$

$$R_{\mu\nu} - \frac{1}{2}g_{\mu\nu}R = \frac{f(\phi)}{2}\left(F_{\mu\rho}F^\rho_\nu - \frac{1}{4}g_{\mu\nu}F^2\right) + \frac{1}{2}\left[\partial_\mu\phi\partial_\nu\phi - \frac{1}{2}g_{\mu\nu}(\partial\phi)^2 - g_{\mu\nu}V(\phi)\right]. \tag{2.9}$$

Since we are going to study the thermodynamical properties of QCD at finite temperature using the gauge/gravity correspondence, we consider the following blackening ansatz of the background metric in the Einstein frame:

$$ds^2 = \frac{e^{2A(z)}}{z^2}\left[-g(z)dt^2 + d\vec{x}^2 + \frac{dz^2}{g(z)}\right], \tag{2.10}$$

$$\phi = \phi(z), \qquad A_\mu = (A_t(z), \vec{0}, 0), \tag{2.11}$$

where $z = 0$ corresponds to the conformal boundary of the five-dimensional spacetime and $g(z)$ stands for the blackening factor. Here we have set the radius of AdS_5 to be unity by scale invariance.

Plugging the ansatz in Eqs. (2.10)–(2.11) into the equations of motion (2.7)–(2.9) leads to the following equations of motion for the background fields:

$$\phi'' + \left(\frac{g'}{g} + 3A' - \frac{3}{z}\right)\phi' + \left(\frac{z^2 e^{-2A} A_t'^2 f_\phi}{2g} - \frac{e^{2A} V_\phi}{z^2 g}\right) = 0, \tag{2.12}$$

$$A_t'' + \left(\frac{f'}{f} + A' - \frac{1}{z}\right)A_t' = 0, \tag{2.13}$$

$$A'' - A'^2 + \frac{2}{z}A' + \frac{\phi'^2}{6} = 0, \tag{2.14}$$

$$g'' + \left(3A' - \frac{3}{z}\right)g' - e^{-2A} z^2 f A_t'^2 = 0, \tag{2.15}$$

$$A'' + 3A'^2 + \left(\frac{3g'}{2g} - \frac{6}{z}\right)A' - \frac{1}{z}\left(\frac{3g'}{2g} - \frac{4}{z}\right) + \frac{g''}{6g} + \frac{e^{2A} V}{3z^2 g} = 0. \tag{2.16}$$

Next, we specify the physical boundary conditions to solve Eqs. (2.12)–(2.16). We impose the conditions that the metric in the string frame is asymptotic to AdS_5 at the boundary $z = 0$ and the black hole solutions are regular at the horizon $z = z_H$.

(i) $z \to 0$:

$$A(0) + \sqrt{\frac{1}{6}}\phi(0) = 0, \qquad g(0) = 1. \tag{2.17}$$

(ii) $z = z_H$:

$$A_t(z_H) = g(z_H) = 0. \tag{2.18}$$

It is natural to introduce the concepts of chemical potential μ and baryon density ρ in QCD from the temporal component of the gauge field A_t using the holographic dictionary of the gauge/gravity correspondence,

$$A_t(z) = \mu + \rho z^2 + O(z^4). \tag{2.19}$$

As mentioned in the Introduction, one of the crucial properties of soft-wall holographic QCD models is that the vector-meson spectrum satisfies the linear Regge trajectories at zero temperature and zero density, i.e., $\mu = \rho = 0$. This issue was first addressed in the soft-wall model [11] using the method of AdS/QCD duality.

We consider the five-dimensional probe vector field V in the action (2.3). The equation of motion for the vector field reads

$$\nabla_\mu [f(\phi) F_V^{\mu\nu}] = 0. \tag{2.20}$$

Following Ref. [11], we first use the gauge invariance to fix the gauge $V_z = 0$; then, the equation of motion of the transverse vector field V_μ ($\partial^\mu V_\mu = 0$) in the background (2.10) reduces to

$$-\psi_i'' + U(z)\psi_i = \left(\frac{\omega^2}{g^2} - \frac{p^2}{g}\right)\psi_i, \tag{2.21}$$

where we have Fourier transformed the vector field V_i as

$$V_i(x, z) = \int \frac{d^4k}{(2\pi)^4} e^{ik\cdot x} v_i(z), \tag{2.22}$$

and further redefined the functions $v_i(z)$ with

$$v_i = \left(\frac{z}{e^A f g}\right)^{1/2} \psi_i \equiv X\psi_i, \tag{2.23}$$

with the potential function

$$U(z) = \frac{2X'^2}{X^2} - \frac{X''}{X}. \tag{2.24}$$

In the case of zero temperature and zero chemical potential, we expect that the discrete spectrum of the vector mesons obeys the linear Regge trajectories. Equation (2.21) reduces to a Schrödinger equation,

$$-\psi_i'' + U(z)\psi_i = m^2\psi_i, \tag{2.25}$$

where $-m^2 = k^2 = -\omega^2 + p^2$. To produce the discrete mass spectrum with the linear Regge trajectories, the potential $U(z)$ should be in a certain form. A simple choice is to fix the gauge kinetic function as

$$f(z) = e^{\pm cz^2 - A(z)}, \tag{2.26}$$

which causes the potential to be

$$U(z) = -\frac{3}{4z^2} - c^2 z^2. \tag{2.27}$$

The Schrödinger equation (2.25) with the potential in Eq. (2.27) has the discrete eigenvalues

$$m_n^2 = 4cn, \tag{2.28}$$

which is linear in the energy level n, which is expected for a vector spectrum at zero temperature and zero density (known as the linear Regge trajectories) [27].

Once we fix the gauge kinetic function $f(z)$, the equations of motion (2.13)–(2.16) can be analytically solved as

$$\phi'(z) = \sqrt{-6\left(A'' - A'^2 + \frac{2}{z}A'\right)}, \tag{2.29}$$

$$A_t(z) = \mu \frac{e^{cz^2} - e^{cz_H^2}}{1 - e^{cz_H^2}}, \tag{2.30}$$

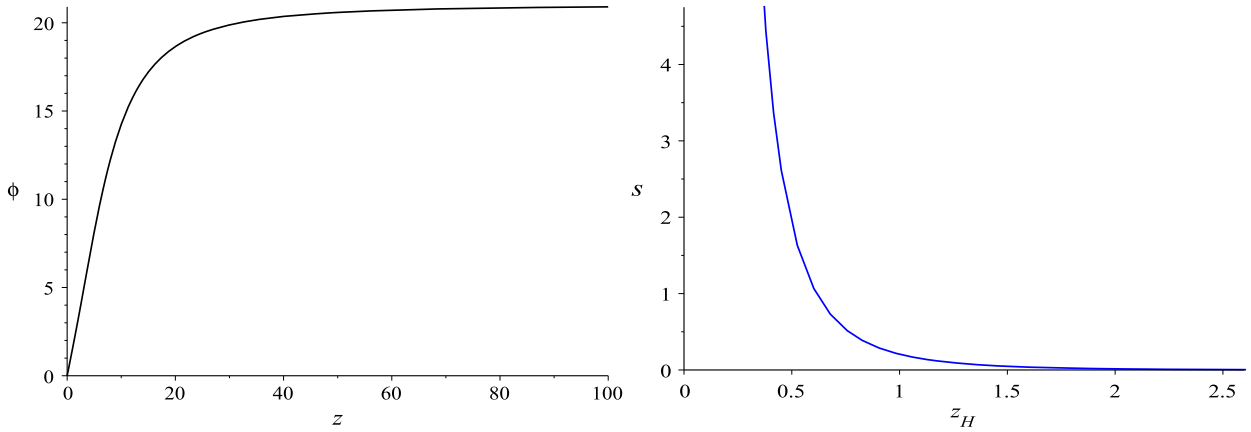

FIG. 3. (a) The neutral scalar field ϕ is a positive, well-defined function of z for a suitable choice of the parameters of the warp factor A. (b) The black hole entropy monotonously decreases as the horizon increases.

$$g(z) = 1 - \frac{1}{\int_0^{z_H} y^3 e^{-3A} dy}\left[\int_0^z y^3 e^{-3A} dy - \frac{2c\mu^2}{(1-e^{cz_H^2})^2}\begin{vmatrix} \int_0^{z_H} y^3 e^{-3A} dy & \int_0^{z_H} y^3 e^{-3A} e^{cy^2} dy \\ \int_{z_H}^{z} y^3 e^{-3A} dy & \int_{z_H}^{z} y^3 e^{-3A} e^{cy^2} dy \end{vmatrix}\right], \tag{2.31}$$

$$V(z) = -3z^2 g e^{-2A}\left[A'' + 3A'^2 + \left(\frac{3g'}{2g} - \frac{6}{z}\right)A' - \frac{1}{z}\left(\frac{3g'}{2g} - \frac{4}{z}\right) + \frac{g''}{6g}\right]. \tag{2.32}$$

Equation (2.29)–(2.32) represent a family of solutions for the black hole background depending on the warp factor $A(z)$, which could be an arbitrary function which satisfies the boundary condition in Eq. (2.17). Furthermore, we also need to ensure that the expression under the square root in Eq. (2.29) is positive for $z \in (z, z_H)$ to guarantee a real scalar field $\phi(z)$. The simple choice $A(z) = az^2 + bz^4$ with $a, b < 0$ was used to study the phase structure of heavy quarks in holographic QCD in Ref. [24]. In Ref. [25], a similar form was used to study the phase structure of light quarks in holographic QCD, but the scalar field $\phi(z)$ becomes complex for some z. In this work, we choose the warp factor $A(z)$ as

$$A(z) = -a\ln(bz^2 + 1). \tag{2.33}$$

Plugging Eq. (2.33) into Eq. (2.29), it is easy to show that the scalar field $\phi(z)$ is always real for positive a and b, as shown in Fig. 3(a). By fitting the mass spectrum of the ρ meson with its excitations (as in Ref. [25]) and comparing the phase transition temperature with the lattice calculation, we can determine the parameter in Eq. (2.28) as $c = 0.227$. The parameters a and b in Eq. (2.33) can be determined by fitting the confinement-deconfinement phase transition temperature at zero chemical potential with $a = 4.046$ and $b = 0.01613$.

III. PHASE STRUCTURE OF THE BLACK HOLE BACKGROUND

In this section, we will explore the phase structure of the black hole background in Eqs. (2.29)–(2.32) that we obtained in the last section. The entropy density and the Hawking temperature can be calculated as

$$s = \left.\frac{\sqrt{g(\vec{x})}}{4}\right|_{z_H}, \qquad T = \frac{g'(z_H)}{4\pi}, \tag{3.1}$$

where $g(\vec{x})$ represents the metric of the internal space along $\vec{x}$. The free energy in the grand canonical ensemble can be obtained from the first law of thermodynamics,

$$F = \epsilon - Ts - \mu\rho, \tag{3.2}$$

where ϵ labels the internal energy density. Comparing the free energies between different sizes of black holes at the same temperature with a certain finite value for the chemical potential, we are able to obtain the phase structure of black holes which corresponds to the phase structure in holographic QCD due to the AdS/CFT correspondence.

A. Black hole thermodynamics

The entropy density, defined in Eq. (3.1), can be easily obtained for our black hole background in Eqs. (2.29)–(2.32),

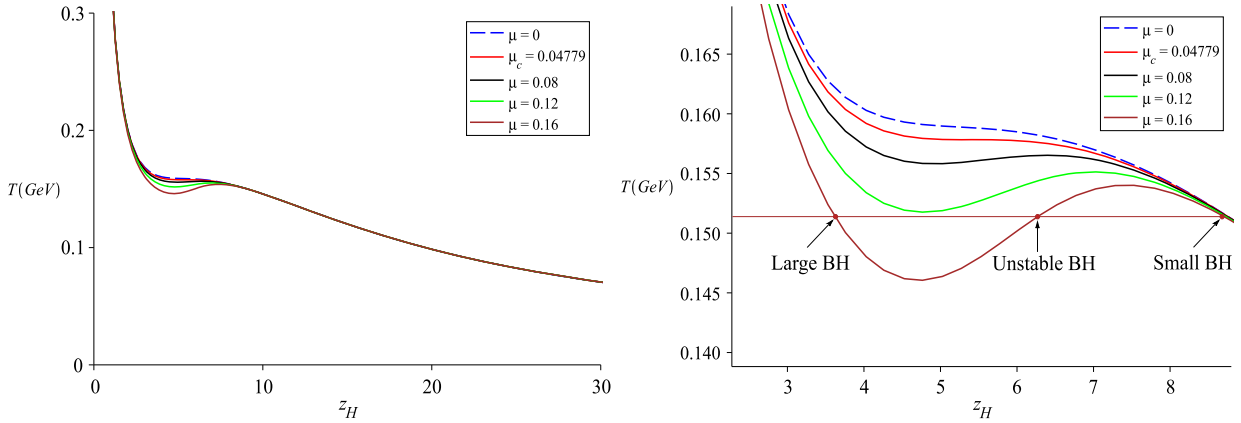

FIG. 4. (a) The black hole temperature vs the horizon at different chemical potentials, where $\mu_c = 0.04779$ GeV. The phase transition region is enlarged in panel (b) to display structural details.

$$s = \frac{e^{3A(z_H)}}{4z_H^3}, \tag{3.3}$$

which is plotted in Fig. 3(b). We see that the entropy density monotonously decreases function as the horizon increases. Based on the second law of thermodynamics, this implies that our black hole background prefers a smaller size with a larger entropy. It is worth mentioning that a smaller value for the horizon is related to a larger size for the black hole.

Another crucial thermal quantity in studying phase transitions is the black hole temperature, also defined in Eq. (3.1), which can be calculated for our black hole background as

$$T = \frac{z_H^3 e^{-3A(z_H)}}{4\pi \int_0^{z_H} y^3 e^{-3A} dy} \times \left[1 - \frac{2c\mu^2 (e^{cz_H^2} \int_0^{z_H} y^3 e^{-3A} dy - \int_0^{z_H} y^3 e^{-3A} e^{cy^2} dy)}{(1 - e^{cz_H^2})^2}\right]. \tag{3.4}$$

The temperature as a function of the horizon, at various chemical potentials, is plotted in Fig. 4. At small chemical potential, $0 \le \mu < \mu_c$, the temperature behaves as a monotonous function of the horizon and decreases to zero as the horizon goes to infinity. It is clear that there is no phase transition because of the monotonous behavior of the temperature. At large chemical potential, $\mu \ge \mu_c$, the temperature becomes multivalued. At each fixed temperature, there are three possible states of black holes. The middle one is thermodynamically unstable due to its negative specific heat [see Eq. (3.9) and Fig. 7(c)]. The other two black holes with different sizes are both thermodynamically stable. To determine which one is dynamically favored, we need to compare their free energies at every temperature and chemical potential. This implies that there could be a phase transition between the two black holes.

In order to determine the transition temperatures at each chemical potential $T_{BB}(\mu)$ between the large black holes and the small black hole, we have to compute the free energy in the grand canonical ensemble from the first law of thermodynamics. At fixed volume, we have

$$dF = -sdT - \rho d\mu. \tag{3.5}$$

Thus, the free energy for a given chemical potential μ can be evaluated by an integral,

$$F = -\int sdT = \int_{zH}^{\infty} s(z_H) T'(z_H) dz_H, \tag{3.6}$$

where we have normalized the free energy of the black holes to vanish at $z_H \to \infty$, i.e., $T = 0$, which is equal to the free energy of the thermal gas. The free energy vs the temperature at various chemical potentials is plotted in Fig. 5(a). The intersection of the free energy implies that there exists a phase transition between two black holes with different sizes at the temperature $T = T_{BB}$.

For $\mu > \mu_c$, the free energy has a swallow-tail shape and shrinks to a singular point at $\mu = \mu_c$, then disappears for $\mu < \mu_c$. The behavior of the free energy implies that the system undergoes a first-order phase transition at each fixed chemical potential $\mu > \mu_c$ and ends at the critical end point (μ_c, T_c) where the phase transition becomes second order. For $\mu < \mu_c$, the phase transition reduces to a crossover. The phase diagram of the black hole to black hole phase transition is plotted in Fig. 5(b), which is consistent with the phase diagram for light quarks obtained in lattice QCD simulations [2].

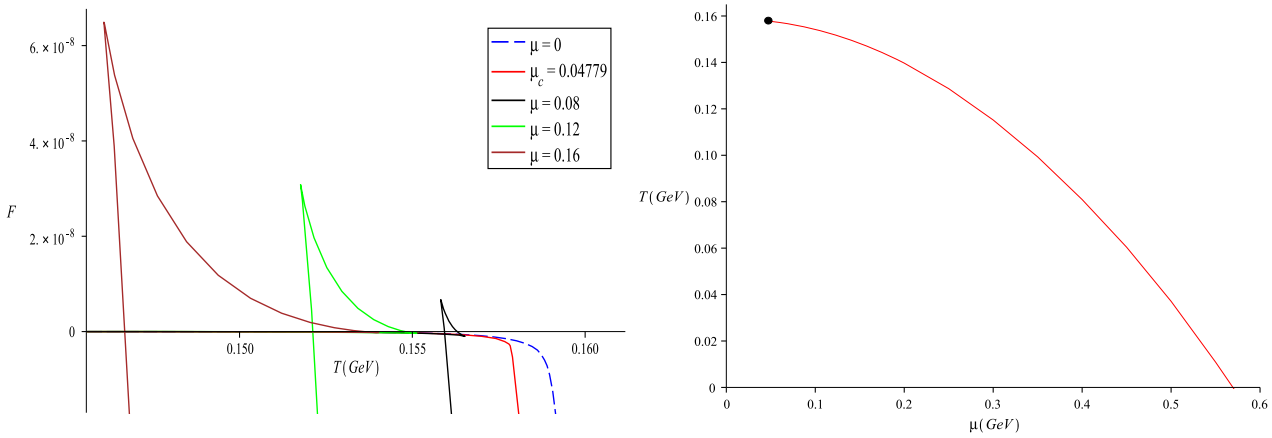

(a) (b)

FIG. 5. (a) The free energy vs the temperature at various chemical potentials. The free energy behaves as a multivalued function of temperature; it has a swallow-tail shape at $\mu > \mu_c$ and becomes monotonous at $\mu < \mu_c$. (b) The phase diagram in the T-μ plane. For large chemical potential $\mu > \mu_c$, the system undergoes a first-order phase transition at a finite temperature and ends at the critical end point $(\mu_c, T_c) \simeq (0.04779, 0.1578)$. For small chemical potential $0 \leq \mu < \mu_c$, the phase transition reduces to a crossover. The zero-temperature phase transition is located at $\mu_{T=0} = 0.5695$.

B. Susceptibility and equations of state

To justify the phase transition, we consider the susceptibility and equations of state in the following. The susceptibility is defined as

$$\chi = \left(\frac{\partial \rho}{\partial \mu}\right)_T. \tag{3.7}$$

We plot the baryon density ρ vs the chemical potential μ in Fig. 6. When $T < T_c$, the multivalued behavior indicates that there is a phase transition at certain values of the chemical potential. However, there is no transition for $T > T_c$, since ρ is a single-valued function of μ. At the critical temperature T_c, the position where the slope becomes infinity is located at the critical point (μ_c, T_c) for the second phase transition, which is consistent with our previous result by comparing free energies between black holes with different sizes.

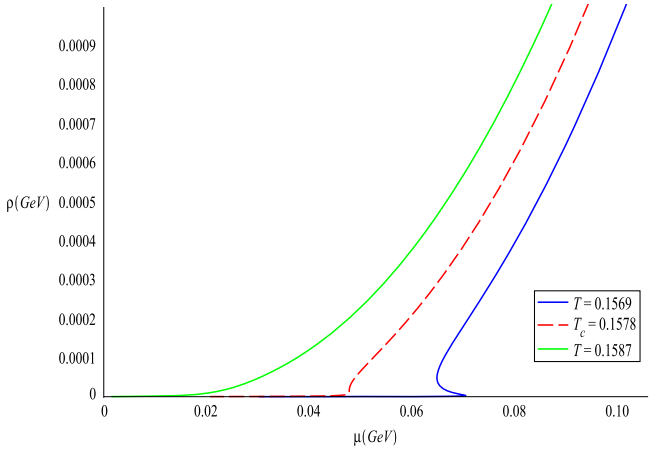

FIG. 6. The baryon density ρ vs the chemical potential μ for various temperatures near the critical point. For $T < T_c$, ρ is multivalued, while for $T > T_c$ it is single valued. At $T = T_c$ the slope is infinite at middle.

The normalized entropy density s/T^3 vs the temperature T is plotted in Fig. 7(a). The normalized entropy density becomes large in the high-temperature limit. The enlarged plot shows that the normalized entropy density is monotonous for $\mu < \mu_c$ and multivalued for $\mu > \mu_c$.

In the grand canonical ensemble with fixed chemical potential, the squared speed of sound can be calculated as

$$c_s^2 = \frac{s}{T\left(\frac{\partial s}{\partial T}\right)_\mu + \mu\left(\frac{\partial \rho}{\partial T}\right)_\mu}, \tag{3.8}$$

which is plotted in Fig. 7(b). The positive/negative part of c_s^2 corresponds to the dynamical stable/unstable black hole. More precisely, the imaginary part of c_s indicates the Gregory-Laflamme instability [42,43], which is closely related to the Gubser-Mitra conjecture that the dynamical stability of a horizon is equivalent to the thermodynamic stability [44–46]. c_s^2 is always positive for $0 \leq \mu < \mu_c$, and reaches zero at the critical point μ_c, T_c. It is worth noticing that c_s^2 approaches the conformal limit $1/3$ in the high-temperature limit for every chemical potential μ.

One of the important quantities to realize the thermodynamic stability is the specific heat capacity, which is defined as

$$C_v = T\left(\frac{\partial s}{\partial T}\right) = \frac{s}{c_s^2}. \tag{3.9}$$

The normalized specific heat capacity C_v/T^3 vs the temperature T is plotted in Fig. 7(c). For $0 \leq \mu < \mu_c$, C_v

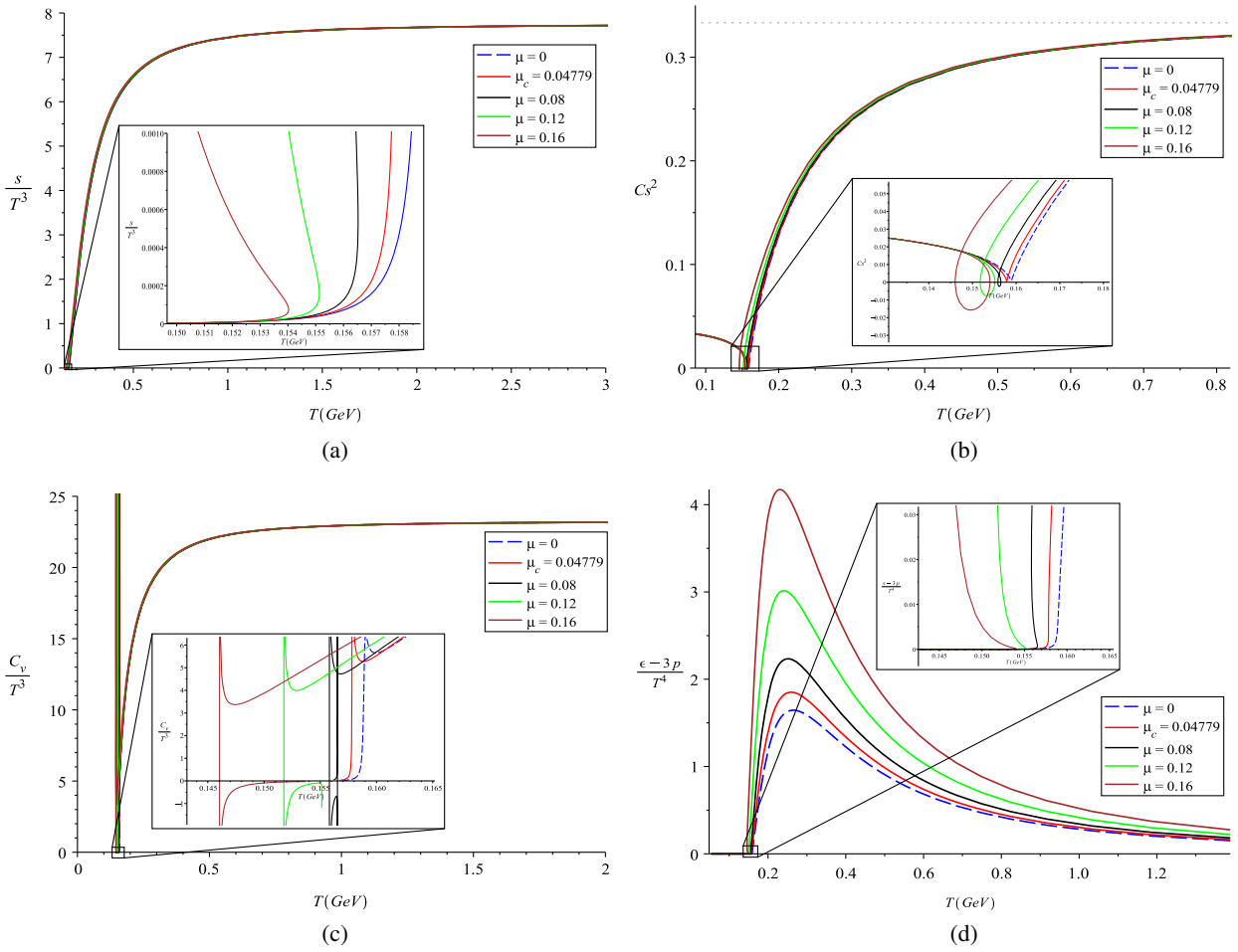

FIG. 7. The normalized entropy (a), speed of sound (b), specific heat (c), and trace anomaly (d) vs the temperature at various chemical potentials.

is always positive, indicating that the black holes are thermodynamically stable. On the other hand, as $\mu > \mu_c$, C_v reveals the negative part which corresponds to thermodynamic instability. Furthermore, C_v and c_s^2 have exactly the same sign behavior. Therefore, the imaginary part of the speed of sound corresponds to the negative part of the specific heat capacity, which implies that our system satisfies the Gubser-Mitra conjecture.

The trace anomaly $\epsilon - 3p$ is another important thermodynamic quantity which can be derived from the internal energy,

$$\epsilon = F + Ts + \mu\rho. \tag{3.10}$$

We plot the normalized trace anomaly $(\epsilon - 3p)/T^4$ vs the temperature T in Fig. 7(d). As the chemical potential decreases, the peak of the trace anomaly decreases and the multivalued behavior becomes single valued.

Finally, we summarize the behaviors of some important thermodynamic quantities in Table I.

IV. OPEN STRINGS IN THE BACKGROUND

Now we will study the phase structure of our holographic QCD model by adding probe open strings to the black hole

TABLE I. The significant patterns in the black hole phase transition.

Figure	$\mu > \mu_c$	$\mu = \mu_c$	$\mu < \mu_c$
$T - z_H$	vibrating	converges to a saddle point	monotonous
$F - T$	swallow-tail	gathers to a point	monotonous
$c_s^2 - T$	knot	shrinks to a cusp	monotonous
$\rho - \mu$	waving	narrows to an infinite slope	monotonous
$T - \mu$	first phase trans.	second phase trans.	crossover

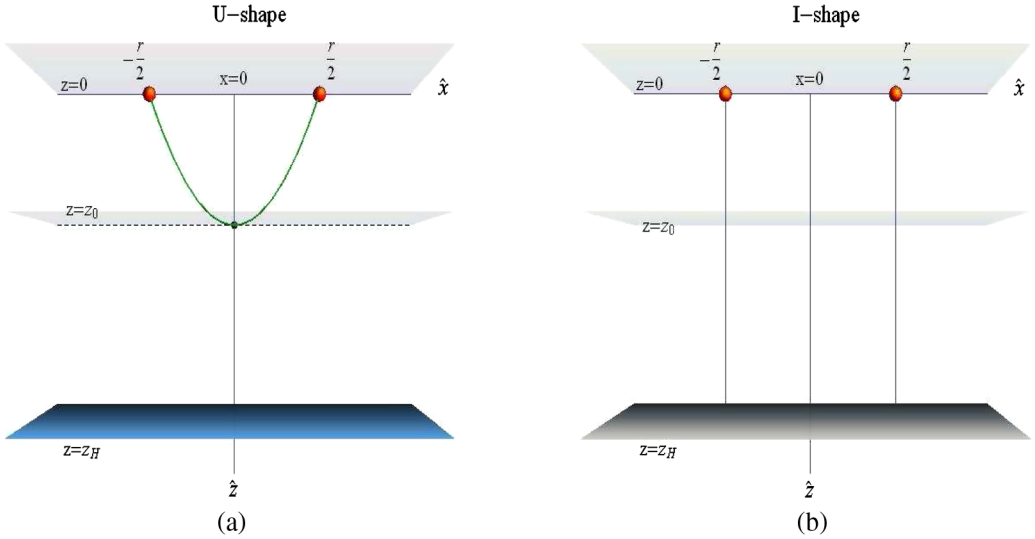

FIG. 8. Two configurations of an open string in a black hole background. (a) Both ends of the open string of the U-shaped configuration are connected to the boundary $z = 0$ and reaches a maximum depth at $z = z_0$. This configuration corresponds to a quark-antiquark bound state at the boundary. (b) The open string of the I-shaped configuration is connected to the boundary and the horizon at $z = z_H$. This configuration corresponds to a single quark/antiquark in the holographic QCD model.

backgrounds in Eqs. (2.29)–(2.32). We consider open strings in the black hole background with their ends attached to the boundary of the bulk at $z = 0$ or the black hole horizon at $z = z_H$. We find that there are two configurations for an open string in the black hole background. One is a U-shaped configuration with the open string reaching its maximum depth at $z = z_0$ and both of its ends attached to the boundary, and the other is an I-shaped configuration with the straight open string having its two ends attached to the boundary and the horizon, respectively. The two configurations are shown in Fig. 8. Since the holographic QCD fields live on the boundary of the black hole background, it is natural to interpret the two ends of the open string as a quark-antiquark pair. The U-shaped configuration corresponds to a quark-antiquark pair being connected by a string and can be identified as a meson state, while the I-shaped configuration corresponds to a free quark or antiquark.

The Nambu-Goto action of an open string is

$$S_{NG} = \int d^2\xi\sqrt{-G}, \tag{4.1}$$

where the induced metric

$$G_{ab} = g_{\mu\nu}\partial_a X^\mu \partial_b X^\nu \tag{4.2}$$

on the two-dimensional world sheet that the string sweeps out as it moves with coordinates (ξ^0, ξ^1) is the pullback of the five-dimensional target spacetime metric $g_{\mu\nu_s}$,

$$ds^2 = \frac{e^{2A_s(z)}}{z^2}\left(g(z)dt^2 + d\vec{x}^2 + \frac{1}{g(z)}dz^2\right), \tag{4.3}$$

where we consider the Euclidean metric to study the thermal properties of the system to identify the black hole temperature of a gravitational theory in the bulk as a thermal field theory on the boundary.

A. Wilson loop

It is known that one can read off the energy of such a quark-antiquark pair from the expectation value of the Wilson loop [30,37,41],

$$\langle W(\mathcal{C})\rangle \sim e^{-V_{q\bar{q}}(r,T)/T}, \tag{4.4}$$

where the rectangular Wilson loop $\mathcal{C}$ is along the directions (t, x) on the boundary of the AdS space attached by the quark-antiquark pair separated by r, and $V(r, T)$ is the quark-antiquark potential.

Based on the string/gauge correspondence, if we consider that a quark-antiquark pair at $(z = 0, x = \pm r/2)$ are connected by an open string (as in Fig. 9), the expectation value of the Wilson loop is given by

$$\langle W(\mathcal{C})\rangle \simeq e^{-S_{\text{on-shell}}}, \tag{4.5}$$

where $S_{\text{on-shell}}$ is the on-shell string action on a world sheet bounded by a loop $\mathcal{C}$ at the boundary of AdS space, which is proportional to the minimum area of the string world sheet. Comparing Eq. (4.4) and Eq. (4.5), the free energy of the meson can be calculated as

$$V_{q\bar{q}}(r, T) = TS_{\text{on-shell}}(r, T). \tag{4.6}$$

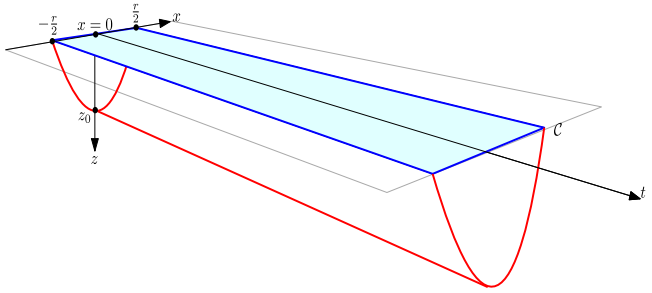

FIG. 9. The Wilson loop $\mathcal{C}$ could be viewed as the boundary of string world-sheet.

B. Configurations of open strings

The string world-sheet action is defined in Eq. (4.1) with the induced metric on the string world sheet in Eq. (4.2). For the U-shaped configuration, by choosing static gauge $\xi^0 = t$, $\xi^1 = x$, the induced metric in the string frame becomes

$$\begin{aligned} ds^2 &= G_{ab} d\xi^a d\xi^b \\ &= \frac{e^{2A_s(z)}}{z^2} g(z) dt^2 + \frac{e^{2A_s(z)}}{z^2}\left(1 + \frac{z'^2}{g(z)}\right) dx^2, \end{aligned} \tag{4.7}$$

where the prime denotes a derivative with respect to x. The Lagrangian and Hamiltonian can be calculated as

$$\mathcal{L} = \frac{e^{2A_s(z)}}{z^2}\sqrt{g(z) + z'^2}, \qquad \mathcal{H} = -\frac{e^{2A_s(z)}}{z^2}\frac{g(z)}{\sqrt{g(z) + z'^2}}. \tag{4.8}$$

Given the boundary conditions

$$z\left(x = \pm\frac{r}{2}\right) = 0, \qquad z(x = 0) = z_0, \qquad z'(x = 0) = 0, \tag{4.9}$$

we obtain the conserved energy from the Hamiltonian in Eq. (4.8)

$$\mathcal{H}(x = 0) = -\frac{e^{2A_s(z_0)}}{z_0^2}\sqrt{g(z_0)}. \tag{4.10}$$

Therefore, the U-shaped configuration of an open string can be solved by

$$z' = \sqrt{g\left(\frac{\sigma^2(z)}{\sigma^2(z_0)} - 1\right)}, \tag{4.11}$$

where σ is the effective string tension [32],

$$\sigma(z) = \frac{e^{2A_s(z)}\sqrt{g(z)}}{z^2}, \tag{4.12}$$

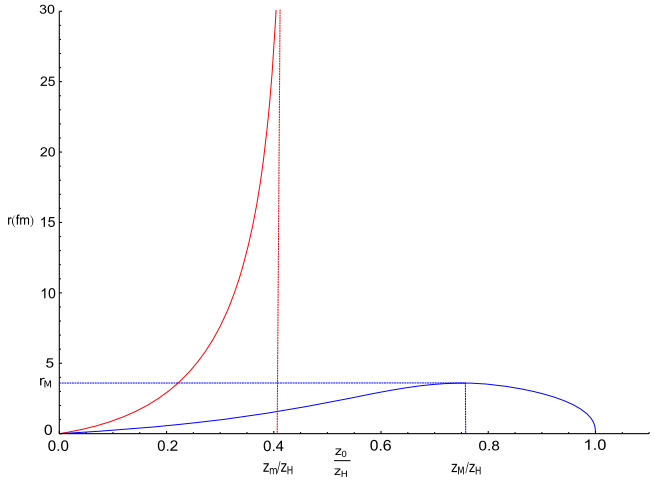

FIG. 10. The distance between the quark and antiquark r vs the maximum depth z_0 of the open string in the U-shaped configuration. The red and blue lines are for $z_H = 9.0$ and $z_H = 3.5$ at $\mu = 0.12$, which represents the small and large black hole, respectively.

and the warp factor in the string frame becomes

$$A_s(z) = A(z) + \sqrt{\frac{1}{6}}\phi(z). \tag{4.13}$$

The distance r between the quark-antiquark pair can be calculated as

$$r = \int_{-\frac{r}{2}}^{\frac{r}{2}} dx = 2\int_0^{z_0} dz \frac{1}{z'} = 2\int_0^{z_0} dz \left[g(z)\left(\frac{\sigma^2(z)}{\sigma^2(z_0)} - 1\right)\right]^{\frac{1}{2}}, \tag{4.14}$$

where z_0 is the maximum depth that the string can reach. The dependence of the distance r on z_0 in two different cases is plotted in Fig. 10. The red (upper) line corresponds to the case of a small black hole horizon where the open string reaches a maximum depth z_m when $r \to \infty$ and cannot reach the horizon, while the blue (lower) line corresponds to the case of a large black hole horizon where the open string might reach the horizon but with a limited separation $r \leq r_M$.

C. Cornell potential

The potential between a quark-antiquark pair $V_{q\bar{q}}$ in Eq. (4.6) for the open strings in U-shaped configurations can be calculated as

$$V_{q\bar{q}} = TS_{\text{on-shell}} = \int_{-\frac{r}{2}}^{\frac{r}{2}} dx \mathcal{L} = 2\int_0^{z_0} dz \frac{\sigma(z)}{\sqrt{g(z)}}\left[1 - \frac{\sigma^2(z_0)}{\sigma^2(z)}\right]^{-\frac{1}{2}}. \tag{4.15}$$

It is well known that the potential $V_{q\bar{q}}$ can be expressed in the form of the Cornell potential, which behaves as a

Coulomb-type potential for short separations between the quark and antiquark, but shows linear behavior for large separations (with the coefficient σ_s being the string tension),

$$V_{q\bar{q}} = -\frac{\kappa}{r} + \sigma_s r + C. \tag{4.16}$$

As $r \to 0$, i.e., $z_0 \to 0$, we expand the distance r and the potential $V_{q\bar{q}}$ at $z_0 = 0$,

$$r = 2\int_0^{z_0} dz \left[g(z)\left(\frac{\sigma^2(z)}{\sigma^2(z_0)} - 1\right)\right]^{-\frac{1}{2}} = r_1 z_0 + O(z_0^2), \tag{4.17}$$

$$V_{q\bar{q}} = 2\int_0^{z_0} dz \frac{\sigma(z)}{\sqrt{g(z)}}\left[1 - \frac{\sigma^2(z_0)}{\sigma^2(z)}\right]^{-\frac{1}{2}} = \frac{V_{-1}}{z_0} + O(1), \tag{4.18}$$

where[1]

$$r_1 = 2\int_0^1 dv \left(\frac{1}{v^4} - 1\right)^{-\frac{1}{2}} = \frac{1}{2}B\left(\frac{3}{4}, \frac{1}{2}\right), \tag{4.19}$$

$$V_{-1} = 2\int_0^1 \frac{dv}{v^2}(1 - v^4)^{-\frac{1}{2}} = \frac{1}{2}B\left(-\frac{1}{4}, \frac{1}{2}\right), \tag{4.20}$$

which gives the Coulomb potential

$$V_{q\bar{q}} = \frac{r_1 V_{-1}}{r} + \cdots, \tag{4.21}$$

with the coefficient

$$\kappa = -r_1 V_{-1} \simeq 1.4355, \tag{4.22}$$

which is a universal constant independent of the choice of the warp factor $A(z)$. We note that, for simplicity, we ignore a factor $1/4\pi\alpha'$ in the Nambu-Goto action (4.1). To compare with the result of lattice QCD, we need to recover the factor to get $\kappa \simeq 1.4355/4\pi\alpha' \simeq 0.114$ for $\alpha' \sim 1$. In Ref. [47], the coefficient of the Coulomb potential was obtained in lattice QCD with $\kappa = 4\alpha_s/3 \simeq 0.133$ for the QCD coupling constant $\alpha_s \sim 0.1$, which is consistent with our result. As $r \to \infty$, i.e., $z_0 \to z_m$, we make a coordinate transformation $z = z_0 - z_0 w^2$. The distance r and the potential $V_{q\bar{q}}$ become

$$r = 2\int_0^1 f_r(w)dw, \qquad V = 2\int_0^1 f_V(w)dw, \tag{4.23}$$

where

$$f_r(w) = 2z_0 w\left[g(z_0 - z_0 w^2)\left(\frac{\sigma^2(z_0 - z_0 w^2)}{\sigma^2(z_0)} - 1\right)\right]^{-\frac{1}{2}}, \tag{4.24}$$

$$f_V(w) = 2z_0 w\frac{\sigma(z_0 - z_0 w^2)}{\sqrt{g(z_0 - z_0 w^2)}}\left[1 - \frac{\sigma^2(z_0)}{\sigma^2(z_0 - z_0 w^2)}\right]^{-\frac{1}{2}}. \tag{4.25}$$

From Fig. 10, the distance r is divergent at $z_0 = z_m$. By careful analysis, we find that this divergence also happens for the quark potential because both of the integrands $f_r(w)$ and $f_V(w)$ are divergent near the lower limit $w = 0$, i.e., $z = z_0 \to z_m$. To study the behaviors of the distance r and potential $V_{q\bar{q}}$ near $z_0 = z_m$, we expand $f_r(w)$ and $f_V(w)$ at $w = 0$,

$$f_r(w) = 2z_0\left[-2z_0 g(z_0)\frac{\sigma'(z_0)}{\sigma(z_0)}\right]^{-\frac{1}{2}} + O(w), \tag{4.26}$$

$$f_V(w) = 2z_0\sigma(z_0)\left[-2z_0 g(z_0)\frac{\sigma'(z_0)}{\sigma(z_0)}\right]^{-\frac{1}{2}} + O(w). \tag{4.27}$$

The integrals in Eq. (4.23) can be approximated by only considering the leading terms of $f_r(w)$ and $f_r(w)$ near $z_0 = z_m$ in Eqs. (4.26)–(4.27). This leads to

$$r(z_0) \simeq 4z_0\left[-2z_0 g(z_0)\frac{\sigma'(z_0)}{\sigma(z_0)}\right]^{-\frac{1}{2}}, \tag{4.28}$$

$$V(z_0) \simeq 4z_0\sigma(z_0)\left[-2z_0 g(z_0)\frac{\sigma'(z_0)}{\sigma(z_0)}\right]^{-\frac{1}{2}} = \sigma(z_0)r(z_0). \tag{4.29}$$

From the above expression, we obtain the expected linear potential $V = \sigma_s r$ at long distances, with the string tension

$$\sigma_s = \left.\frac{dV}{dr}\right|_{z_0=z_m} = \left.\frac{dV/dz_0}{dr/dz_0}\right|_{z_0=z_m} = \left.\frac{\sigma'(z_0)r(z_0) + \sigma(z_0)r'(z_0)}{r'(z_0)}\right|_{z_0=z_m} = \sigma(z_m). \tag{4.30}$$

The temperature dependence of the string tension for various chemical potentials is plotted in Fig. 11. We see that the string tension decreases when the temperature increases. At the confinement-deconfinement transformation temperature T_μ, the system transforms to the deconfinement phase and the string tension suddenly drops to zero, as we expected [48]. The behavior is consistent with the results of lattice QCD simulations [48]. In Fig. 11, $\mu_c = 0.04779$ is the critical chemical potential for the black hole

[1]We require the property of the beta function $\frac{B(x/k,y)}{k} = \int_0^1 dt t^{x-1}(1-t^k)^{y-1}$.

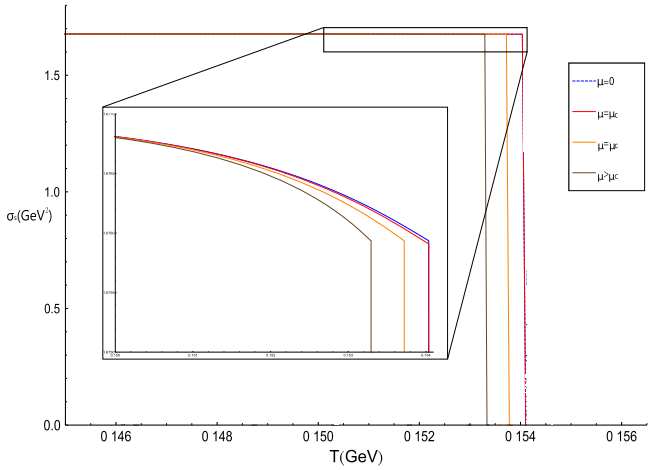

FIG. 11. The string tension σ_s vs the temperature for different chemical potentials with $\mu_c = 0.04779$ and $\mu_c' = 0.1043$. The region near the phase transition is enlarged, where the tension suddenly drops to zero, implying the phase transition between confinement and deconfinement phases.

phase transition in the background and $\mu_c' = 0.1043$ is the critical chemical potential for the confinement-deconfinement phase transition in our holographic QCD model. We will discuss these two phase transitions in detail in the next section.

We therefore showed that the behaviors of the quark potential at short distances and long distances agree with the form of the Cornell potential [49],

$$V(r) = -\frac{\kappa}{r} + \sigma_s r + C, \tag{4.31}$$

which has been measured in great detail in lattice simulations [50]. In order to obtain the r dependence of $V_{q\bar{q}}$, we will evaluate the integral in Eq. (4.16), which is divergent due to the fact that integrand is not well defined at $z = 0$. We regularize $V_{q\bar{q}}$ by subtracting the divergent terms as

$$V_{q\bar{q}}^{[R]} = C(z_0) + 2\int_0^{z_0} dz \left[\frac{\sigma(z)}{\sqrt{g(z)}}\left[1 - \frac{\sigma^2(z_0)}{\sigma^2(z)}\right]^{-\frac{1}{2}} - \frac{1}{z^2}[1 + 2A_s'(0)z]\right], \tag{4.32}$$

where

$$C(z_0) = -\frac{2}{z_0} + 4A_s'(0)\ln z_0. \tag{4.33}$$

The regularized potentials are plotted in Fig. 12. For $T < T_\mu$, $V_{q\bar{q}}^{[R]}$ has the form of the Cornell potential with linear behavior for large r. For $T > T_\mu$, the open string breaks at a certain distance and $V_{q\bar{q}}^{[R]}$ become constant for larger distances.

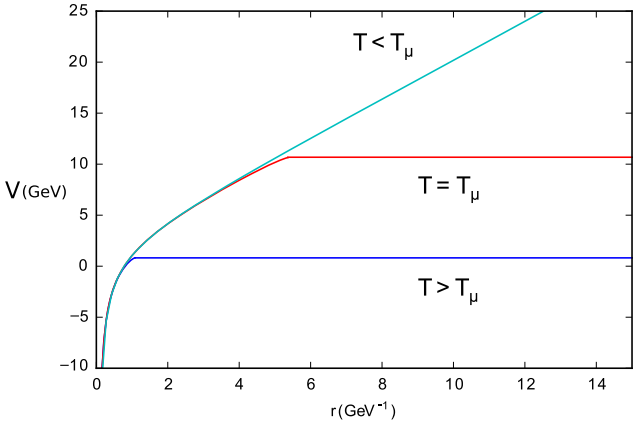

FIG. 12. The regularized heavy quark potential $V_{q\bar{q}}^{[R]}$ vs r at $\mu = 0.12$ GeV for $z_H = \{1, 3, 10\}$ (from bottom to top).

V. PHASE DIAGRAM

In the previous sections, we have constructed a holographic QCD model by studying the Einstein-Maxwell-scalar system. We obtained a family of black hole backgrounds and studied the phase transition between the black holes by computing their free energies. We also added probe open strings in the black hole backgrounds and studied the different string configurations at various temperatures, which corresponded to the confinement and deconfinement phases in the dual holographic QCD model. In this section, we are ready to discuss the phase diagram of QCD by combining the phase structure of the black hole background and the configurations of the probe open strings in the black hole background. We have obtained the phase diagram for the phase transitions of the black hole background (as shown in Fig. 5) by comparing the free energies of black holes. We schematically summarize our results in Fig. 13. As the black hole temperature grows, the black hole horizon grows as well, i.e., z_H decreases. At the phase transition temperature, the small black hole with horizon z_{H_s} jumps to the large one with horizon z_{H_l}.

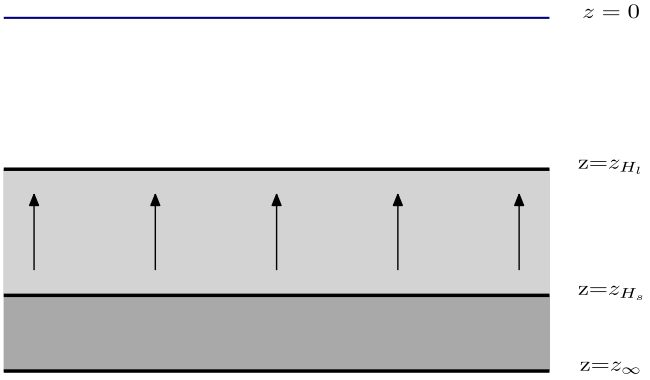

FIG. 13. Schematic diagram of the phase transition from a small black hole z_{H_s} to a large black hole z_{H_l}.

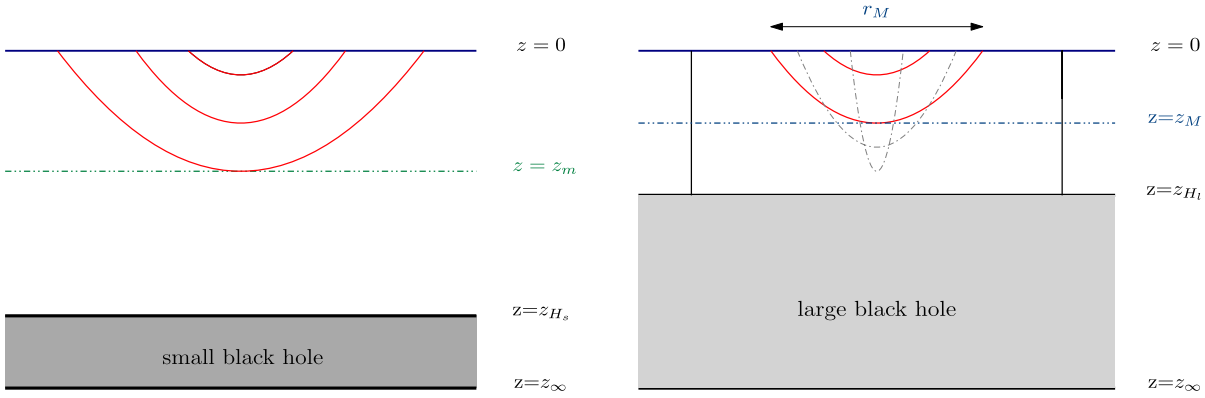

FIG. 14. Small/large black hole in the horizon description, $z_{H_{s/l}}$.

A. Probe strings and the dynamical wall

To see the confinement-deconfinement phase transition, we added probe open strings to the black hole background. As shown in Fig. 10, for a small black hole z_{H_s}, the separation of the bounded quark-antiquark pair r can be as long as possible, but the depth of the string is limited by a maximum value z_m, which we call the dynamical wall. In this case, the open strings are always connected in the U-shaped configurations to form bounded states and the system is in the confinement phase. The dynamical wall is the crucial concept in understanding the confinement-deconfinement phase transition in holographic QCD models. On the other hand, for a large black hole z_{H_l} (as shown in Fig. 10), the separation of the quark-antiquark pair is bounded by a maximum distance r_M at the depth z_M. If the distance between the quark and antiquark is longer than r_M, a U-shaped string will break into two I-shaped open strings attached between the boundary and the horizon. In this case, a free quark or antiquark might exist, indicating that the system is in the deconfinement phase. The open string breaking process corresponds to the melting of the bounded state [51].

Our discussion is summarized in Fig. 14. For a small black hole [as shown in Fig. 14(a)] there exists a dynamical wall so that open strings are always U-shaped, corresponding to the confinement phase. However, for a large black hole [as shown in Fig. 14(b)] the open strings could be either U-shaped or I-shaped depending on the distance between the quark and antiquark, corresponding to the deconfinement phase. The configurations of open strings are collected in Table II. Since the black hole temperature is closely associated with the black hole horizon, we expect that the system will undergo a phase transition from confinement to deconfinement when the temperature increases.

TABLE II. Black hole sizes and open string configurations with respect to the $q\bar{q}$ separation r.

Black hole size	U-shape	I-shape	Phase in QCD
Small (z_{H_s})	$0 < r < \infty$	none	Confinement
Large (z_{H_l})	$r < r_M$	$r > r_M$	Deconfinement

Since the role of the dynamical wall is crucial to affirm the confinement phase in holographic QCD models, let us examine it carefully. To determine the position of the dynamical wall z_m, we use the fact that $r(z_m) \to \infty$, which leads to the equation $\sigma'(z_m) = 0$. With the definition of the string tension in Eq. (4.12), we have

$$\frac{g'(z_m)}{4g(z_m)} + A_s'(z_m) + \frac{1}{z_m} = 0. \tag{5.1}$$

In the confinement phase, the value of the horizon z_H is large, so that $g(z)$ is almost a constant and $g'(z) \sim 0$. We thus have

$$A_s'(z_m) + \frac{1}{z_m} = 0. \tag{5.2}$$

We would like to remark that the position of the dynamical wall z_m is almost a universal value, and does not depend on either the chemical potential or the temperature.[2] In our particular model with the choice of $A(z)$ in Eq. (2.33) and also the string frame A_s in Eq. (4.13), the position of the dynamical wall z_m can be obtained as

$$z_m = \sqrt{\frac{a - 1 - \sqrt{a(a-4)}}{b(2a+1)}} \simeq 4.22. \tag{5.3}$$

For each chemical potential μ, we draw the effective string tension σ for black holes with three different horizons in Fig. 15(a). For a small black hole $z_{H_s} < z_{H_\mu}$, σ is single

[2]Here we mean that the system is in the confinement phase. In the deconfinement phase, there is no dynamical wall.

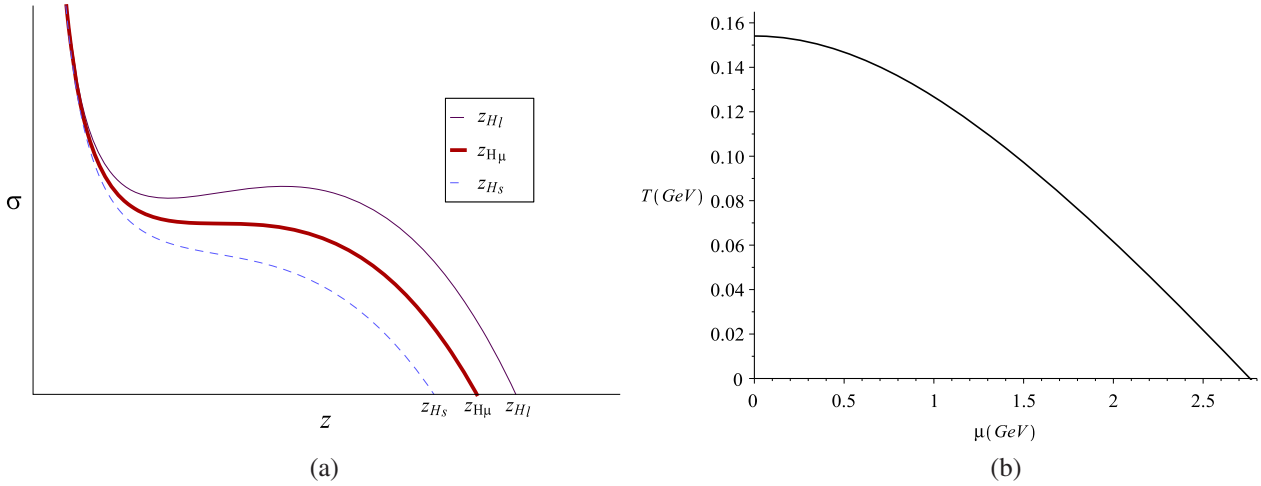

FIG. 15. (a) The effective string tension σ for black holes with different horizons. (b) The transformation temperature T_μ, associated with z_{H_μ}, at which the dynamical wall appears/disappears for each chemical potential. The T intercept $T_0 = 0.1541$ GeV.

valued, while for a large black hole $z_{H_l} > z_{H_\mu}$, σ becomes multivalued. We define the transformation temperature T_μ at chemical potential μ as the temperature corresponding to the critical black hole horizon z_{H_μ}. At the transformation temperature, the dynamical wall appears/disappears as we decrease/increase the temperature. The transformation temperature is associated to the transformation between the confinement and deconfinement phases in the holographic QCD. The transformation temperature T_μ at each chemical potential is plotted in Fig. 15(b). We should emphasize that the transformation between the confinement and deconfinement phases here is not a phase transition. The confinement phase smoothly transforms to the deconfinement phase as the temperature increases gradually.

B. Confinement-deconfinement phase diagram

To obtain the completed phase diagram in our holographic QCD model, we combine the phase transition between large and small black holes as well as the different configurations of the probe open strings in the background. In Fig. 16(a), the black (dotted) line represents the confinement-deconfinement transformation, while the red (solid) line is the phase transition between black holes. Once the phase transition from a small black hole at lower temperature to a large black hole at higher temperature takes place, the black hole horizon jumps to a large value which is beyond the critical black hole horizon zH_μ and the system undergoes the confinement-deconfinement phase transition. The intersection of the two lines is identified as the critical point at $(\mu_c' = 0.1043, T_c' = 0.1538)$. In terms of the baryon chemical potential $\mu_B \simeq 3\mu_c' = 0.313$, the critical point we found is consistent with the recent result from lattice QCD [52]: $\mu_B \leq 2T_c'$ and $0.135\ \text{GeV} \leq T_c' \leq 0.155\ \text{GeV}$.

The final phase diagram of the confinement-deconfinement phase transition is plotted in 16(b). For a large chemical potential $\mu > \mu_c'$, there is a first-order confinement-deconfinement

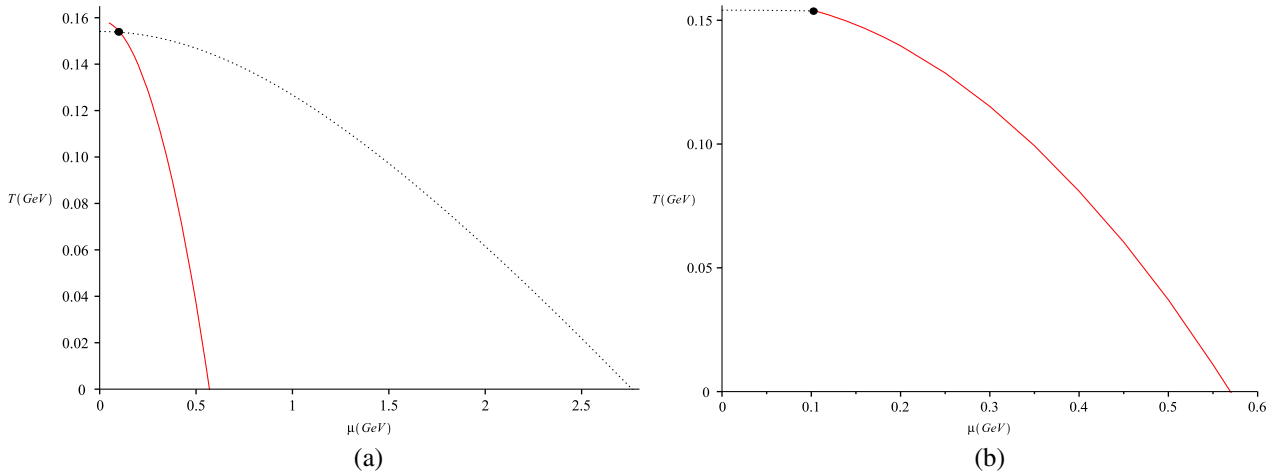

FIG. 16. The phase diagram of a probing string in a black hole system; the intersection is at $(\mu_c' = 0.1043, T_c' = 0.1538)$ GeV.

phase transition at the temperature T_μ (shown as a solid red line). At the critical point $\mu = \mu_c'$ and $T = T_c'$ (shown as a black dot), the first-order phase transition weakens to a second-order phase transition. For small chemical potential $\mu < \mu_c'$, the confinement-deconfinement phase transition reduces to a smooth crossover (shown as a dotted black line).

VI. CONCLUSION

In this paper, we constructed a bottom-up holographic QCD model by studying gravity coupled to a $U(1)$ gauge field and a neutral scalar in five-dimensional spacetime, i.e., a five-dimensional Einstein-Maxwell-scalar system. By solving the equations of motion analytically, we obtained a family of black hole solutions which depend on two arbitrary functions $f(z)$ and $A(z)$. Different choices of the functions $f(z)$ and $A(z)$ correspond to different black hole backgrounds. To include meson fields in QCD, probe gauge fields were added to the five-dimensional backgrounds. The function $f(z)$ can be fixed by requiring the linear Regge spectrum for mesons. By making a suitable choice of the function $A(z)$ [as in Eq. (2.33)], we fixed our holographic QCD model.

We obtained the phase structure of the black hole background by studying its thermodynamic quantities. To realize the confinement-deconfinement phase transition in QCD, we added probe open strings in the black hole background and studied the shape of their stable configurations. Different U-shaped and I-shaped configurations were identified for confinement and deconfinement phases, respectively. By combining the phase structure of the black hole background and the U-shaped to I-shaped transformation of the open strings, we obtained the phase diagram of the confinement-deconfinement phase transition in our holographic QCD model. In our model, the critical point—where the first-order phase transition becomes a crossover—is predicted to be at (0.1043 GeV, 0.1538 GeV), which is consistent with the recent lattice QCD result in Ref. [52].

We studied the Wilson loop in QCD by calculating the world-sheet area of an open string based on the holographic correspondence. The heavy quark potential can be obtained from the Wilson loop. We obtained the Cornell potential which has been well studied using lattice QCD. The diagram of the heavy quark potentials at different temperatures is plotted in Fig. 17. At low temperature $T < T_\mu$, the potential is linear at large r, corresponding to the confinement phase; at high temperature $T > T_\mu$, the potential becomes constant at large r, corresponding to the deconfinement phase. There is a phase transition at $T = T_\mu$, as shown in the figure.

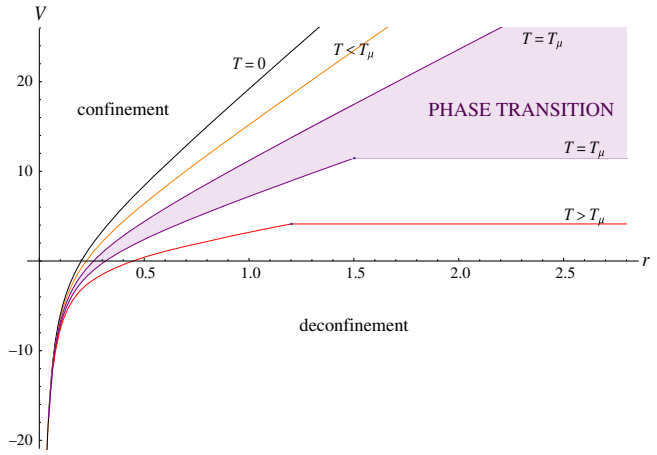

FIG. 17. The heavy quark potential at various temperatures.

The main properties of our holographic QCD model are as follows:

(i) The coupled Einstein-Maxwell-scalar system was solved analytically to obtain a family of black hole backgrounds in Eqs. (2.29)–(2.32).
(ii) The meson spectrum in our model satisfies the linear Regge behavior [as in Eq. (2.28)].
(iii) For finite chemical potentials $\mu > \mu_c$, the background exhibits a phase transition between a small black hole and a large black hole, as shown in Fig. 5(b).
(iv) The dynamical wall appears/disappears for small/large black holes, which implies the confinement-deconfinement phase transition. In addition, in the confinement phase, the position of the dynamical wall is nearly constant [as in Eq. (5.3)] and independent of the chemical potential and temperature.
(v) We obtained the Cornell form of the quark potential in Eq. (4.31) by calculating the Wilson loop.

ACKNOWLEDGMENTS

We would like to thank Rong-Gen Cai, Song He, Mei Huang, Danning Li, Xiaofeng Luo, and Xiaoning Wu for useful discussions. This work is supported by the Ministry of Science and Technology (MOST 105-2112-M-009-010) and the National Center for Theoretical Science, Taiwan.

[1] N. Cabibbo and G. Parisi, Exponential hadronic spectrum and quark liberation, Phys. Lett. **59B**, 67 (1975).
[2] O. Philipsen, Lattice QCD at non-zero temperature and baryon density, arXiv:1009.4089.
[3] P. Petreczky, Lattice QCD at non-zero temperature, J. Phys. G **39**, 093002 (2012).
[4] J. M. Maldacena, The large N limit of superconformal field theories and supergravity, Int. J. Theor. Phys. **38**, 1113 (1999).
[5] M. Kruczenski, D. Mateos, R. C. Myers, and D. J. Winters, Meson spectroscopy in AdS/CFT with flavor, J. High Energy Phys. 07 (2003) 049.
[6] J. Babington, J. Erdmenger, N. J. Evans, Z. Guralnik, and I. Kirsch, Chiral symmetry breaking and pions in nonsupersymmetric gauge/gravity duals, Phys. Rev. D **69**, 066007 (2004).
[7] M. Kruczenski, D. Mateos, R. C. Myers, and D. J. Winters, Towards a holographic dual of large $N(c)$ QCD, J. High Energy Phys. 05 (2004) 041.
[8] T. Sakai and S. Sugimoto, Low energy hadron physics in holographic QCD, Prog. Theor. Phys. **113**, 843 (2005).
[9] T. Sakai and S. Sugimoto, More on a holographic dual of QCD, Prog. Theor. Phys. **114**, 1083 (2005).
[10] J. Erlich, E. Katz, D. T. Son, and M. A. Stephanov, QCD and a Holographic Model of Hadrons, Phys. Rev. Lett. **95**, 261602 (2005).
[11] A. Karch, E. Katz, D. T. Son, and M. A. Stephanov, Linear confinement and AdS/QCD, Phys. Rev. D **74**, 015005 (2006).
[12] S. Kobayashi, D. Mateos, S. Matsuura, R. C. Myers, and R. M. Thomson, Holographic phase transitions at finite baryon density, J. High Energy Phys. 02 (2007) 016.
[13] B. Batell and T. Gherghetta, Dynamical soft-wall AdS/QCD, Phys. Rev. D **78**, 026002 (2008).
[14] S. S. Gubser and A. Nellore, Mimicking the QCD equation of state with a dual black hole, Phys. Rev. D **78**, 086007 (2008).
[15] W. de Paula, T. Frederico, H. Forkel, and M. Beyer, Dynamical AdS/QCD with area-law confinement and linear Regge trajectories, Phys. Rev. D **79**, 075019 (2009).
[16] C. Charmousis, B. Goutéraux, B. Kim, E. Kiritsis, and R. Meyer, Effective holographic theories for low-temperature condensed matter systems, J. High Energy Phys. 11 (2010) 151.
[17] U. Gursoy, E. Kiritsis, L. Mazzanti, G. Michalogiorgakis, and F. Nitti, Improved holographic QCD, Lect. Notes Phys. **828**, 79 (2011).
[18] O. DeWolfe, S. S. Gubser, and C. Rosen, A holographic critical point, Phys. Rev. D **83**, 086005 (2011).
[19] D. Li, S. He, M. Huang, and Q.-S. Yan, Thermodynamics of deformed AdS_5 model with a positive/negative quadratic correction in graviton-dilaton system, J. High Energy Phys. 09 (2011) 041.
[20] O. DeWolfe, S. S. Gubser, and C. Rosen, Dynamic critical phenomena at a holographic critical point, Phys. Rev. D **84**, 126014 (2011).
[21] M. Mia, K. Dasgupta, C. Gale, and S. Jeon, A holographic model for large N thermal QCD, J. Phys. G **39**, 054004 (2012).
[22] M. Fromm, J. Langelage, S. Lottini, and O. Philipsen, The QCD deconfinement transition for heavy quarks and all baryon chemical potentials, J. High Energy Phys. 01 (2012) 042.
[23] R.-G. Cai, S. Chakrabortty, S. He, and L. Li, Some aspects of QGP phase in a hQCD model, J. High Energy Phys. 02 (2013) 068.
[24] S. He, S.-Y. Wu, Y. Yang, and P.-H. Yuan, Phase structure in a dynamical soft-wall holographic QCD model, J. High Energy Phys. 04 (2013) 093.
[25] Y. Yang and P.-H. Yuan, A refined holographic QCD model and QCD phase structure, J. High Energy Phys. 11 (2014) 149.
[26] Y. Yang and P.-H. Yuan, Confinement-deconfinement phase transition for heavy quarks, J. High Energy Phys. 12 (2015) 161.
[27] M. Shifman, Highly Excited Hadrons in QCD and Beyond, arXiv:hep-ph/0507246.
[28] S.-J. Rey, S. Theisen, and J.-T. Yee, Wilson-Polyakov loop at finite temperature in large N gauge theory and anti–de Sitter supergravity, Nucl. Phys. **B527**, 171 (1998).
[29] A. Brandhuber, N. Itzhaki, J. Sonnenschein, and S. Yankielowicz, Wilson loops in the large N limit at finite temperature, Phys. Lett. B **434**, 36 (1998).
[30] O. Andreev and V. I. Zakharov, Heavy-quark potentials and AdS/QCD, Phys. Rev. D **74**, 025023 (2006).
[31] H. Boschi-Filho, N, and R. F. Braga, AdS/CFT correspondence and strong interactions, *Proc. Sci.*, IC2006 (2006) 035.
[32] O. Andreev and V. I. Zakharov, On heavy-quark free energies, entropies, Polyakov loop, and AdS/QCD, J. High Energy Phys. 04 (2007) 100.
[33] C. D. White, The Cornell potential from general geometries in AdS/QCD, Phys. Lett. B **652**, 79 (2007).
[34] J. L. Albacete, Y. V. Kovchegov, and A. Taliotis, Heavy quark potential at finite temperature using the holographic correspondence, Phys. Rev. D **78**, 115007 (2008).
[35] S. He, M. Huang, and Q.-S. Yan, Logarithmic correction in the deformed AdS_5 model to produce the heavy quark potential and QCD beta function, Phys. Rev. D **83**, 045034 (2011).
[36] P. Colangelo, F. Giannuzzi, and S. Nicotri, Holography, heavy-quark free energy, and the QCD phase diagram, Phys. Rev. D **83**, 035015 (2011).
[37] R.-G. Cai, S. He, and D. Li, A hQCD model and its phase diagram in Einstein-Maxwell-Dilaton system, J. High Energy Phys. 03 (2012) 033.
[38] D. Li, M. Huang, and Q.-S. Yan, A dynamical holographic QCD model for chiral symmetry breaking and linear confinement, Eur. Phys. J. C **73**, 2615 (2013).
[39] Y. Wu, D. Hou, and H.-c. Ren, Some comments on the holographic heavy quark potential in a thermal bath, arXiv:1401.3635.
[40] O. Andreev, Color screening masses from string models, Phys. Rev. D **94**, 126003 (2016).
[41] J. M. Maldacena, Wilson Loops in Large N Field Theories, Phys. Rev. Lett. **80**, 4859 (1998).
[42] R. Gregory and R. Laflamme, Black Strings and p-Branes are Unstable, Phys. Rev. Lett. **70**, 2837 (1993).

[43] R. Gregory and R. Laflamme, The instability of charged black strings and p-branes, Nucl. Phys. **B428**, 399 (1994).

[44] S. S. Gubser and I. Mitra, Instability of charged black holes in anti–de Sitter space, arXiv:hep-th/0009126.

[45] S. S. Gubser and I. Mitra, The evolution of unstable black holes in anti–de Sitter space, J. High Energy Phys. 08 (2001) 018.

[46] H. S. Reall, Classical and thermodynamic stability of black branes, Phys. Rev. D **64**, 044005 (2001).

[47] G. S. Bali, QCD forces and heavy quark bound states, Phys. Rep. **343**, 1 (2001).

[48] M. Mia, Ke. Dasgupta, C. Gale, and S. Jeon, Heavy quarkonium melting in large N thermal QCD, Phys. Lett. B **694**, 460 (2011).

[49] E. Eichten, K. Gottfried, T. Konoshita, K. D. Lane, and T.-M. Yan, Charmonium: The model, Phys. Rev. D **17**, 3090 (1978); Charmonium: Comparison with experiment, Phys. Rev. D **21**, 203 (1980).

[50] G. S. Bali, QCD forces and heavy quark bound states, Phys. Rep. **343**, 1 (2001).

[51] C. Ewerz, O. Kaczmarek, and A. Samberg, Free energy of a heavy quark-antiquark pair in a thermal medium from AdS/CFT, arXiv:1605.07181.

[52] A. Bazavov, H.-T. Ding, P. Hegde, O. Kaczmarek, F. Karsch, E. Laermann, Y. Maezawa, S. Mukherjee, H. Ohno, P. Petreczky, H. Sandmeyer, P. Steinbrecher, C. Schmidt, S. Sharma, W. Soeldner, and M. Wagner, The QCD equation of state to $\mathcal{O}(\mu_B^6)$ from lattice QCD, Phys. Rev. D **95**, 054504 (2017).